Optical and Quantum Electronics (2023) 55:383
https://doi.org/10.1007/s11082-023-04656-5

Calculation of intersubband absorption in n-doped $BaSnO_3$ quantum wells

Novak Stanojević[1] · Nikola Vuković[1,2] · Jelena Radovanović[1,2]

Received: 29 November 2022 / Accepted: 6 February 2023 / Published online: 1 March 2023

Abstract
In this paper, we theoretically investigate intersubband absorption in La-doped $BaSnO_3$/BaO perovskite-oxide double and triple symmetrical quantum wells. The goal is to assess the emerging possibilities offered by perovskite heterostructures for realization of oxide-based quantum well optoelectronic devices. Properties such as small electron effective mass, very high room-temperature mobility of $BaSnO_3$, large conduction band offset between the two materials, are all promising for technological applications. Some of the possible applications include active *n*-channel materials in *p*-*n* junctions, field-effect transistors, ferroelectric field-effect transistors, sensitive UV photoconductors, and electron transport layers in perovskite solar cells. We are interested in tuning of the absorption spectra via quantum well width modulation, changing of doping density and variation of external electric field along the growth direction which is important for application in electro-optical light modulators. The electronic structure is calculated self-consistently by solving the Schrödinger–Poisson system of equations where the exchange correlation effects are also taken into the account.

Keywords Optical devices · Barium stannate · Optical absorption · Intersubband transitions

1 Introduction

Novel and promising perovskite stannate $BaSnO_3$ (BSO) material system with La^{3+}-doping (BLSO) has received considerable attention in recent years due to its high room-temperature electron mobility and electrical conductivity, high optical transparency, and excellent thermal/chemical stability (Kang et al. 2022). BLSO single crystals are reported to have mobilities as high as $320 cm^2/Vs$ at room temperature at a mobile electron concentration of $n = 8 * 10^{19} cm^{-3}$ which belongs to the degenerate regime ($n \gtrsim 10^{19} cm^{-3}$). For this degenerate regime BLSO single crystals have a higher mobility compared to all mainstream

✉ Novak Stanojević
novakstanojevic1@gmail.com

[1] School of Electrical Engineering, University of Belgrade, Bulevar Kralja Aleksandra 73, 11120 Belgrade, Serbia

[2] Centre for Light-Based Research and Technologies COHERENCE, Belgrade, Serbia

semiconductors (Si, GaAs, GaN) (Kim et al. 2012a; Jacoboni et al. 1977; Chin et al. 1994). However because of dislocations the electron mobility for BLSO films on $SrTiO_3$ is smaller compared to BLSO single crystals and GaN. Control of the donor-doping determines the application of the material as either transparent semiconductor or transparent conductor. Demonstrations of $Ba_{1-x}La_xSnO_3$ transparent electronic devices include active *n*-channel materials in the *p*-*n* junctions (Lee et al. 2017) and the field-effect transistors (FETs) (Park et al. 2014), sensitive UV photoconductors (Lee et al. 2021), and electron transport layers in perovskite solar cells (Shin et al. 2017). Excellent structural match of BLSO to ferroelectric and antiferroelectric oxides with the perovskite structure, e.g., $Pb(Zr, Ti)O_3$ could enable BLSO to serve as a high mobility channel for ferroelectric field-effect transistors (Miller and McWhorter 1992; Ma and Han 2002) and yield a subthreshold slope beating the 60 mV/decade Boltzmann limit of conventional field-effect transistors by fabricating negative capacitance field-effect transistors (NCFETs) (Khan et al. 2014; Paik et al. 2017).

Recent studies performed on $BaO/BaSnO_3$ quantum wells (QWs) demonstrate the advantages of perovskite-oxide (PO) based QWs over traditional semiconductor QWs in terms of strong optical nonlinearities (Li et al. 2021; Failed 2021). Techniques for epitaxial growth of perovskite oxides on Si have lately been developed (McKee et al. 1998, 2001; Kumah et al. 2020; Demkov and Posadas 2014), so it has become possible to integrate perovskite-oxide based QWs with Si.

A very large conduction band offset (~ 1.74 eV) (Li et al. 2021) enables greater control of the QW properties and allows barium stannate QWs to be used across a broad spectral range, including exploitation of a giant nonlinear optical susceptibility over THz to near-visible light. In order to optimize the performance of quantum devices based on intersubband transitions and adjust the spectral range in which they operate rigorous modeling of their electronic structure is needed.

In this work we analyze double QW (DQW) and triple QW (TQW) in which the well and barrier layers consist of BSO and BaO materials respectively. Both the DQW and the TQW are surrounded by thick BaO barrier layers. The electronic structure of these QWs is calculated by self-consistently solving the Schrödinger–Poisson system of equations where the exchange correlation effects are also included through the modification of the total effective potential. We then evaluate the fractional absorption and investigate the tuning of absorption spectra with the thickness of the QW layers and the intensity of the external electric field applied along the growth direction of the heterostructure.

2 Theoretical model

For describing these heterostructures we have used effective mass theory since the Luttinger criterion (Luttinger and Kohn 1955) is met. We start from the 1D effective mass Schrödinger equation:

$$-\frac{\hbar^2}{2}\frac{d}{dz}\frac{1}{m^*(z)}\frac{d\psi_i(z)}{dz} + U_{eff}(z)\psi_i(z) = E_i\psi_i(z) \tag{1}$$

where $m^*(z)$ is the effective mass along the growth direction, and $\psi_i(z)$ is the (envelope) wave function. The effective mass changes along the length of the heterostructure for different materials. Due to the large band gap of barium stannate non parabolicity effects would be negligible and are not taken into account. The total effective potential energy:

$$U_{eff}(z) = U_c(z) - e\varphi(z) + U_{xc}(z) - eF_e z \tag{2}$$

consists of $U_c(z)$, which is the conduction band offset between BSO and BaO (~1.74 eV), the added electrostatic potential $\varphi(z)$ due to the La-doping, found by solving the Poisson equation, the exchange correlation potential energy $U_{xc}(z)$ and F_e is the externally applied electric field along the growth direction z.

For the electrostatic potential $\varphi(z)$ the Poisson equation reads:

$$\frac{d^2\varphi(z)}{dz^2} = \frac{e}{\varepsilon^*(z)}\big(n(z) - N_d(z)\big) \tag{3}$$

where $N_d(z)$ is the La-doping density. The assumption has been made as in Li et al. (2021) that the ions of the dopants are evenly distributed across the entire heterostructure. In our simulations we use average doping densities of $N_d = 1 * 10^{19}\text{cm}^{-3}$ and $N_d = 5 * 10^{18}\text{cm}^{-3}$ for the DQW and TQW respectively (Kim et al. 2012b).

Electron density $n(z)$ is given by:

$$n(z) = \sum\nolimits_i N_{s,i}\left|\psi_i(z)\right|^2 \tag{4}$$

where $N_{s,i}$ is the surface carrier density, i.e. number of electrons per unit cross-section area in the i-th state, which can be expressed as:

$$N_{s,i} = \frac{m_{ti}k_BT}{\pi\hbar^2}\ln\left(1 + e^{\frac{E_F - E_i(0)}{k_BT}}\right) \tag{5}$$

Here E_F is the Fermi energy, and m_{ti} is the transversal mass which can be found as an integral over the length of the heterostructure:

$$\frac{1}{m_{ti}} = \int \psi_i^*\big(k_t = 0\big)\frac{1}{m^*(z)}\psi_i\big(k_t = 0\big)dz \tag{6}$$

The local exchange correlation potential energy $U_{xc}(z)$ can be expressed as (Ando et al. 2003):

$$U_{xc}(z) = -\frac{e^4}{32\pi^2\hbar^2}\frac{m^*(z)}{\varepsilon^*(z)^2}\left(\frac{9\pi}{4}\right)^{\frac{1}{3}}\frac{2}{\pi r_s{}^*}\left[1 + 0.0545 r_s{}^*\log\left(1 + \frac{11.4}{r_s{}^*}\right)\right] \tag{7}$$

where $\varepsilon^*(z)$ is the dielectric constant, and $r_s{}^*$ is the average distance between carriers scaled by the effective Bohr radius $a_B^* = \frac{4\pi\varepsilon^*(z)\hbar^2}{m^*(z)e^2}$:

$$r_s{}^*[n(z)] = \sqrt[3]{\frac{3}{4\pi n(z)}}\frac{1}{a_B^*} \tag{8}$$

The total effective potential energy is dependent on the envelope functions (2), so the corresponding coupled Schrödinger–Poisson (SP) system of equations is solved self-consistently (Failed 2022a).

The energies and wave functions of the bound states found from SP solver are further used to calculate the linear optical absorption $A(\hbar\omega)$ for the intersubband transitions.

The perturbation Hamiltonian for the interaction of the electrons in the heterostructure with electromagnetic radiation is taken as:

$$\widehat{H}' = \frac{e}{m_0}\vec{A}\vec{\widehat{p}} \tag{9}$$

where $\vec{A}$ is the magnetic vector potential and $\vec{\widehat{p}}$ is the momentum operator. This perturbation Hamiltonian and its matrix elements are used in Fermi's golden rule for calculating the transition probability per unit time for an electron from state i with energy E_i to state f with energy E_f:

$$w_{if} = \frac{2\pi}{\hbar}\left|H'_{if}\right|^2 \delta\left(E_f - E_i \pm \hbar\omega\right) \tag{10}$$

Due to the confinement of electrons in the QWs along the direction of growth the allowed energies of the electrons belong to subbands. The total probability for transitions between two subband indexed i and j per volume (V) is then obtained via summation over the relevant wave vector components:

$$W_{if} = \frac{1}{V}\sum_{k_x}\sum_{k_x}\frac{2\pi}{\hbar}\left|H'_{if}\right|^2 \delta\left(E_f - E_i \pm \hbar\omega\right)\left[f_{FD}\left(E_i\right)\left(1 - f_{FD}\left(E_f\right)\right) - f_{FD}(E_f)(1 - f_{FD}(E_i))\right] \tag{11}$$

The total absorption coefficient of light passing through a structure can be calculated from $\alpha_{if} = \frac{W_{if}\hbar\omega}{VI}$, which in combination with (11) and some further transformations leads to the total fractional absorption for intersubband transmission from state i to state f:

$$A_{if}(\hbar\omega) = \frac{e^2\omega\pi}{\varepsilon_0 n_r c}\left(N_{s,i} - N_{s,f}\right)\left|d_{if}\right|^2 L(\hbar\omega) \tag{12}$$

where n_r is the refractive index, d_{if} is the dipole matrix element $d_{if} = \int_0^{L_z}\psi_i^* z\psi_f dz$, and L_z is the total length of the structure. The Lorentzian $L(\hbar\omega)$ is expressed as: $L(\hbar\omega) = \frac{1}{2\pi}\Gamma_{if}\Big/\left[\left(E_f(0) - E_i(0) - \hbar\omega\right)^2 + \left(\frac{\Gamma_{if}}{2}\right)^2\right]$ with its width Γ_{if} estimated to be 10% of the energy difference between the final and initial states.

3 Results and discussion

In this section we present the results of our numerical simulations. Since the largest absorption is achieved in symmetric structures, in this paper, we limit our considerations to symmetric QW profiles only. The temperature is taken to be300K, while the used values for the relative dielectric constants are 22.51 (https://materialsproject.org/materials/mp-3163) for $BaSnO_3$ and 34 for BaO (https://www.ucl.ac.uk/~ucapahh/research/crystal/bao.htm). The effective electron mass for $BaSnO_3$ is taken to be $0.17m_0$ as in Li et al. (2021), and $0.31m_0$ for BaO (Medvedeva 2022). The conduction band offset of these two materials 1.74eV as in Li et al. (2021).

We vary the layer's thickness in the multiples of the lattice parameter (unit cell) of BSO which is 0.41nm. Figure 1. shows the results of the SP solver, namely the total effective potential energy $U_{eff}(z)$ and wave functions squared for the symmetric DQW with well thickness (c_w) of 5 unit cells and barrier thickness of 1 unit cell.

The total effective potential energy is denoted by the blue line, while the conduction band offset without bending is denoted by the red dash-dotted line. There are four energy subbands (dashed lines) and the corresponding squared wave functions are shown in Fig. 1.

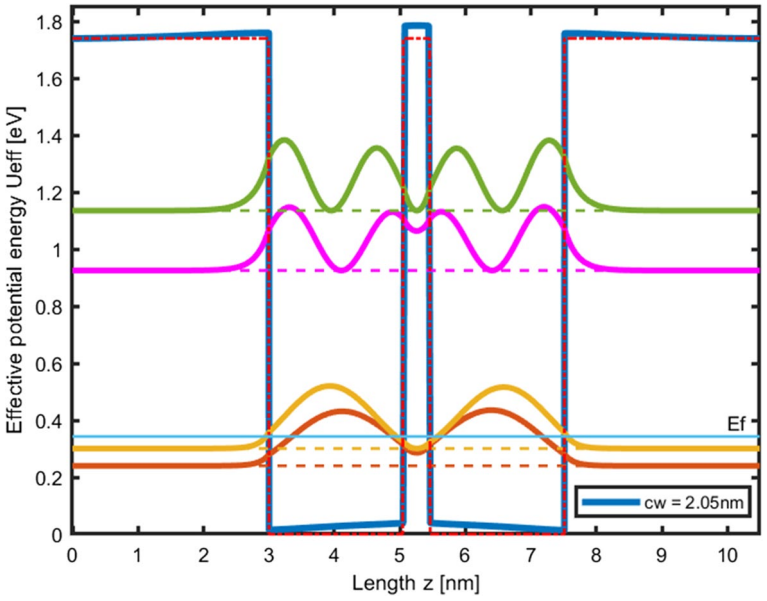

Fig. 1 Conduction-band diagram for a symmetric DQW with the total effective potential energy $U_{eff}(z)$ and the squared wave functions for four energy subbands

The Fermi level is above the second subband and is also shown in Fig. 1. with the bright blue horizontal line.

Figure 2a illustrates the absorption spectra for three values of c_w: 4 unit cells (blue spectrum, full line), 5 unit cells (red spectrum, dashed line), and 6 unit cells (orange spectrum, dash-dotted line). The QWs are separated by a 1 unit cell thick barrier layer in all cases. There are three absorption peaks in the figure, the dominant one is A_{12} (transition between

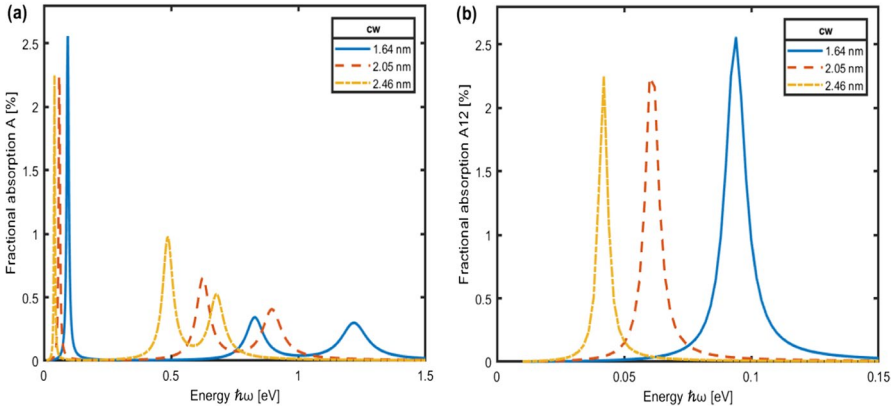

Fig. 2 Absorption spectra for symmetric DQW, **a** with three absorption transitions: A_{12}, A_{23}, A_{14}, and **b** just the dominant absorption transition A_{12}, for well thickness (c_w) being 4, 5 and 6 unit-cells (1.64, 2.05 and 2.46 nm), while the barrier thickness is 1-unit cell (0.41 nm)

the first and the second subband), and the smaller two are A_{23} (transition between the second and the third subband) and A_{14} (transition between the first and the fourth subband). From Fig. 2a we can see that the increase in the QW width results in the decrease of energy at which all three absorption transitions occur. The intensity of the A_{12} transition decreases while the intensity of the other two transitions increases with the increase of the width of the well layers.

Figure 3 illustrates the two dominant absorption transitions A_{12} and A_{23} for two different TQWs. For the first TQW all 3 well layers are 4 unit cells thick (blue spectra, full line), for the second TQW both the left and the right well layer widths are 5 unit cells, while the middle well layer is 4 unit cells thick (red spectra, dash-dotted line). The well layers are separated by two 1 unit cell thick barriers in both cases. From Fig. 3 we see the resulting shift in energies at which absorption transitions A_{12} and A_{23} occur, with the increase in the width of the first and third well layer. The intensity of both the dominant transitions decreases with the increase of the width of the first and third well layer.

The inset of Fig. 3 shows the total effective potential energy $U_{eff}(z)$ and wave functions squared for the first TQW. The Fermi level is just above the second subband and is denoted by the bright blue horizontal line.

Control of the absorption spectrum by changing the intensity of the external electric field along the growth direction is very important for practical use, such as for electro-optical light modulators. The external electric field changes the total effective potential energy and bends the conduction band diagram. This affects the energies of the subbands and their

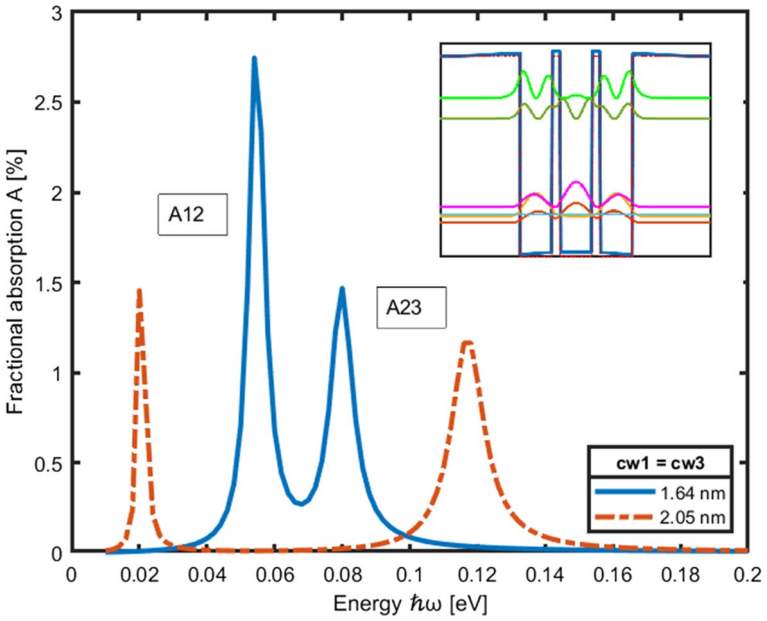

Fig. 3 Absorption spectra for two symmetric TQW, with the dominant A_{12} and A_{23} transitions shown. Both the first and third well layer are four unit cells thick (1.64 nm) for the first TQW, and five unit cells thick (2.05 nm) for the second TQW, while the second well layer is four-unit cell thick (1.64 nm) in both cases. The inset shows the total effective potential energy $U_{eff}(z)$ and wave functions squared that correspond to the first of these two TQWs

wave functions, which in turn changes the dipole matrix elements and the electron surface densities and so alters the absorption spectrum. In order to exploit such devices effectively the energy difference between the bound states needs to change as much as possible with the change of the external electric field, so that such devices can operate at lower voltages.

Figure 4 shows the results of the SP solver, namely the total effective potential energy $U_{eff}(z)$ and square of wave functions for the symmetric DQW with well thickness (c_w) of 5 unit cells and barrier thickness of 1 unit cell.

The total effective potential energy is denoted by the blue line, while the conduction band offset without bending is denoted by the red dash-dotted line. There are three energy subbands (dashed lines) and the corresponding wave functions which are shown in Fig. 4. The Fermi level is above the second subband and is also shown in Fig. 4 with the bright blue horizontal line.

In the case of symmetric structures, like those that are considered in this work, we know from perturbation theory that the bound state energy of the ground state decreases with the increase of the external electrical field. The other bound state energies change much more slowly, and with the increase of the external electric field, they first experience a slight increase and then a decrease for stronger fields. This leads to changes in the energy of the intersubband transitions. The energies for the $1 \rightarrow n$ transitions become larger, while the matrix element for the dominant transition $1 \rightarrow 2$ becomes smaller due to a smaller overlap between the wave functions of the first and second bound state, which in turn reduces the intensity of the absorption A_{12}.

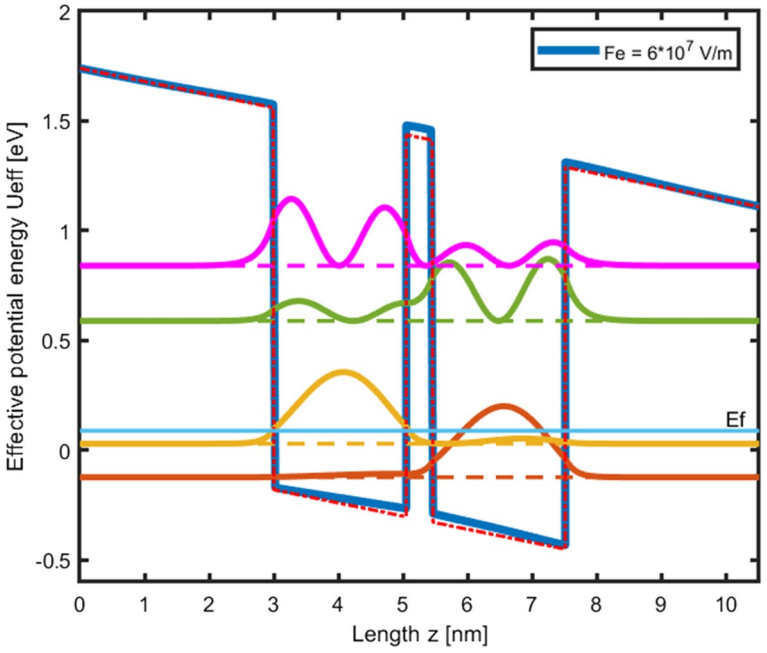

Fig. 4 Conduction-band diagram shows the total effective potential energy $U_{eff}(z)$ and the squared wave functions for four energy subbands for a symmetric DQW with both well layers being 5 unit cells thick (2.05nm) and barrier thickness of 1 unit cell (0.41nm) where the external electric field along the growth direction is $6 * 10^7 \mathrm{V/m}$

The effect of an external electric field on absorption in DQW with well layers five-unit-cells thick, and the barrier layer one-unit thick can be seen in Fig. 5.

The energy of the absorption transition A_{12} increases, while its intensity decreases with the electric field applied in the QWs' growth direction, which is expected from the theoretical consideration stated above.

Finally, we changed the average doping densities of the DQW (the well layers were five-unit-cell thick, and the barrier layer one-unit cell thick) to see the effect that would have on the absorption spectrum, which can be seen in Fig. 6. The doping densities are $N_d = 1 * 10^{19}\text{cm}^{-3}$, $N_d = 3 * 10^{19}\text{cm}^{-3}$ and $N_d = 5 * 10^{19}\text{cm}^{-3}$. In all cases the dopants are assumed to be evenly distributed across the entire heterostructure. There are three absorption peaks in the figure, A_{12}, A_{23} and A_{14}.

For higher doping densities the Fermi level E_F shifts to higher energies which changes the electron surface densities of the bound energy states. This leads to a large change in the absorption spectrum, where A_{23} and A_{14} transitions become larger, and the transition A_{23} becomes the dominant one.

4 Summary

In this work we have focused on the intersubband absorption calculation in QWs realized in n-doped BSO, a promising transparent conductive oxide with superior electron conductivity and wide optical band gap, in order to determine its potential for realization of devices based

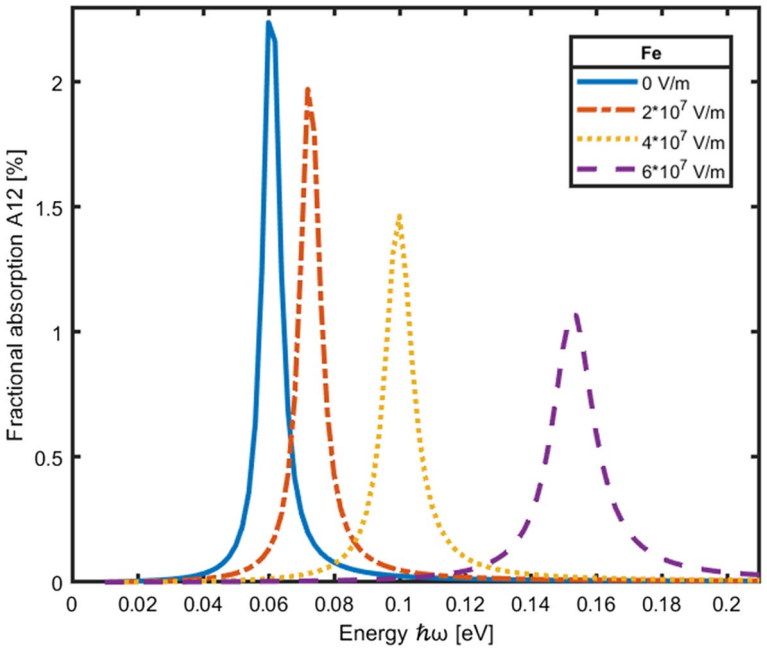

Fig. 5 Absorption spectrum for DQW (the well layers were five-unit-cell thick, and the barrier layer one-unit cell thick), where only the peak A_{12} is shown (the Fermi level is just above the second subband) for different values of external electric field

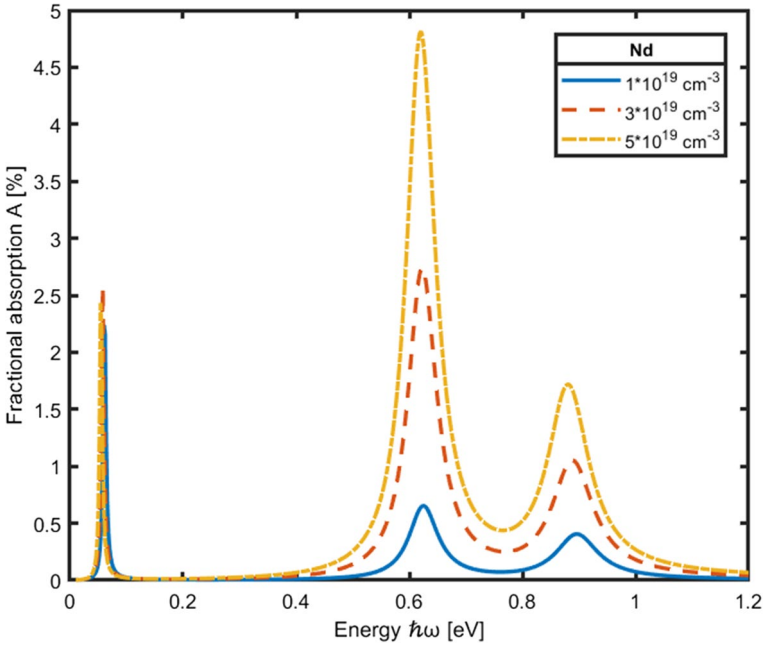

Fig. 6 Absorption spectrum for DQW (the well layers were five-unit-cell thick, and the barrier layer one-unit cell thick) for different values of doping densities

on intersubband transitions. Our initial study presented here suggests that high level of manipulation with absorption spectra is possible by changing layer thickness, doping density and the tuning of the external electrical field.

Author's contributions All authors contributed to the study conception and design. Material preparation, data collection and analysis were performed by all authors. The first draft of the manuscript was written by Novak Stanojević and all the authors contributed in finalizing the previous versions of the manuscript. All authors have read and approved the submitted version of the manuscript.

Funding This work was supported by Ministry of Education, Science and Technological Development (Republic of Serbia).

Data availability Not applicable.

Declarations

Conflict of interest The authors have no relevant financial or non-financial interests to disclose.

Ethical approval Not applicable.

References

Ando, T., Taniyama, H., Ohtani, N., Nakayama, M., Hosoda, M.: Self-consistent calculation of subband occupation and electron–hole plasma effects: variational approach to quantum well states with Hartree and exchange-correlation interactions. J. Appl. Phys. **94**, 4489–4501 (2003)

Barium Oxide, Electronic properties, (https://www.ucl.ac.uk/~ucapahh/research/crystal/bao.htm). Retrieved May 5, 2022.

Chin, V.W.L., Tansley, T.L., Osotchan, T.: Electron mobilities in gallium, indium, and aluminum nitrides. J. Appl. Phys. **75**(11), 7365–7372 (1994)

Demkov, A.A., Posadas, A.B.: Integration of Functional Oxides with Semiconductors. Springer, New York (2014)

Guo, W.: Transition metal oxide thin films integration on $SrTiO_3$, Dissertation (2021).

Jacoboni, C., Canali, C., Ottaviani, G., Quaranta, A.A.: A review of some charge transport properties of silicon. Solid State Electron. **20**(2), 77–89 (1977)

Kang, J., Lee, J.H., Lee, H.K., Kim, K.T., Kim, J.H., Maeng, M.J., Hong, J.A., Park, Y., Kim, K.H.: Effect of threading dislocations on the electronic structure of La-doped $BaSnO_3$ thin films. Mater. (basel). **15**(7), 2417 (2022)

Khan, A.I., Chatterjee, K., Wang, B., Drapcho, S., You, L., Serrao, C., Bakaul, S.R., Ramesh, R., Salahuddin, S.: Negative capacitance in a ferroelectric capacitor. Nat. Mater. **14**, 182–186 (2014)

Kim, H.J., et al.: High mobility in a stable transparent perovskite oxide. Appl. Phys. Express **5**, 061102 (2012a)

Kim, H.J., et al.: Physical properties of transparent perovskite oxide (Ba, La)SnO_3 with high electrical mobility at room temperature. Phys. Rev. B **86**, 165205 (2012b)

Kumah, D.P., Ngai, J.H., Kornblum, L.: Epitaxial oxides on semiconductors: from fundamentals to new devices. Adv. Funct. Mater. **30**, 1901597 (2020)

Laurent Nevou.: Q_SchrodingerPoisson1D_CB, (https://github.com/LaurentNevou/Q_SchrodingerPoisson1D_CB), GitHub. Retrieved March 18 (2022a)

Lee, J.H., Lee, W.-J., Kim, T.H., Lee, T., Hong, S., Kim, K.H.: Transparent *p*-CuI/*n*-BaSnO3-δ heterojunctions with a high rectification ratio. J. Phys. Condens. Matter. **29**, 384004 (2017)

Lee, Y., Yoon, D., Yu, S., Sim, H., Park, Y., Nam, Y.-S., Kim, K.-J., Choi, S.-Y., Kang, Y., Son, J.: Reversible manipulation of photoconductivity caused by surface oxygen vacancies in perovskite stannates with ultraviolet light. Adv. Mater. **34**, 2107650 (2021)

Li, W., Hamze, A.K., Demkov, A.A.: Tunable giant nonlinear optical susceptibility in $BaSnO_3$ quantum wells. Phys. Rev. B **104**, 235419 (2021)

Luttinger, J.M., Kohn, W.: Motion of electrons and holes in perturbed periodic fields. Phys. Rev. **97**, 869 (1955)

Ma, T.P., Han, J.-P.: Why is nonvolatile ferroelectric memory field-effect transistor still elusive? IEEE Electron. Device Lett. **23**, 386–388 (2002)

McKee, R.A., Walker, F.J., Chisholm, M.F.: Crystalline oxides on silicon: the first five monolayers. Phys. Rev. Lett. **81**, 3014 (1998)

McKee, R.A., Walker, F.J., Chisholm, M.F.: Physical structure and inversion charge at a semiconductor interface with a crystalline oxide. Science **293**, 468–471 (2001)

Medvedeva, J.E.: Averaging of the electron effective mass in multicomponent transparent conducting oxides. EPL **78**, 57004 (2007)

Miller, S.L., McWhorter, P.J.: Physics of the ferroelectric nonvolatile memory field effect transistor. J. Appl. Phys. **72**, 5999–6010 (1992)

Paik, H., Chen, Z., Lochocki, E., et al.: Adsorption-controlled growth of La-doped $BaSnO_3$ by molecular-beam epitaxy. APL Mater. **5**, 116107 (2017)

Park, C., Kim, U., Ju, C.J., Park, J.S., Kim, Y.M., Char, K.: High mobility field effect transistor based on $BaSnO_3$ with Al_2O_3 gate oxide. Appl. Phys. Lett. **105**, 203503 (2014)

Shin, S.S., Yeom, E.J., Yang, W.S., Hur, S., Kim, M.G., Im, J., Seo, J., Noh, J.H., Seok, S.I.: Colloidally prepared La-doped $BaSnO_3$ electrodes for efficient, photostable perovskite solar cells. Science **356**, 167–171 (2017)

The Materials Project, $BaSnO_3$ mp-3163 (https://materialsproject.org/materials/mp-3163). Retrieved May 5, 2022.